# Competition between axisymmetric and three-dimensional patterns between exactly counter-rotating disks

C. Nore[a)]
*Université Paris XI, Département de Physique, 91405 Orsay Cedex, France and Laboratoire d'Informatique pour la Mécanique et les Sciences de l'Ingénieur, CNRS, BP 133, 91403 Orsay Cedex, France*

L. Martin Witkowski
*Université Pierre et Marie Curie (Paris VI), 4 place Jussieu, 75252 Paris Cedex 05, France and Laboratoire d'Informatique pour la Mécanique et les Sciences de l'Ingénieur, CNRS, BP 133, 91403 Orsay Cedex, France*

E. Foucault and J. Pécheux
*Laboratoire d'Etudes Aérodynamiques, Boulevard Marie et Pierre Curie, Téléport 2, BP 30179, 86962 Futuroscope Chasseneuil Cedex, France*

O. Daube
*Université d'Evry Val d'Essonne, 40 rue du Pelvoux, 91020 Evry Cedex, France*

P. Le Quéré
*Laboratoire d'Informatique pour la Mécanique et les Sciences de l'Ingénieur, CNRS, BP 133, 91403 Orsay Cedex, France*

(Received 25 July 2005; accepted 11 March 2006; published online 4 May 2006)

The bifurcations and the nonlinear dynamics of the von Kármán swirling flow between exactly counter-rotating disks in a stationary cylinder are numerically and experimentally investigated. The dynamics are governed by two parameters, the radius-to-height ratio $A=R/H$ and the Reynolds number, Re, based on disk rotation speed and cylinder height. The stability analysis performed for $2\leqslant A\leqslant 20$ shows that nonaxisymmetric and axisymmetric modes can be stationary or time dependent in this range. Three-dimensional modes are dominant for $A\leqslant 13.25$ while axisymmetric modes are critical for $A>13.25$. The patterns of the dominant perturbations are analyzed. In the particular case of $A=15$, nonlinear computations are performed at Reynolds numbers slightly above threshold and are compared to experimental results, showing the competition between axisymmetric and three-dimensional modes. © *2006 American Institute of Physics*. [DOI: 10.1063/1.2196090]

## I. INTRODUCTION

The flow above a rotating disk or between coaxial disks in a cylindrical cavity, or von Kármán swirling flow,[1] is one class of flows involving a great variety of complex behaviors, in addition to a large amount of practical applications in rotating machinery. It depends qualitatively on the radius-to-height aspect ratio $A\equiv R/H$, as well as on the ratio $s\equiv\Omega_{\mathrm{low}}/\Omega_{\mathrm{up}}$ of the angular velocities of the upper and lower disks (we choose $\Omega_{\mathrm{up}}>0$). Theoretical study for infinite radius disks traces back to von Kármán,[2] Batchelor,[3] and Stewartson[4] while flow visualization in the case of finite disks has been used to explore the flow structure since 1960.[5]

Most studies have explored the rotor-stator configuration with $s=0$. When $A\gg 1$, instabilities[6–9] are of two sorts: boundary layer instabilities, where structures are observed in the boundary layers, or a bulk instability, where structures extend from one disk to the other one. The former take place in the Ekman and Bödewadt boundary layers, i.e., in the neighborhood of the rotating and the stationary disk, respectively, and produce patterns in the form of propagating circular vortices or spirals. They are of two types (A and B, or II and I) and are thought to be related to the Coriolis force, and to an unstable inflection point, respectively. They have been extensively studied, both experimentally and theoretically, within the framework of the self-similar von Kármán equations for flow above a single rotating disk.[8,10–12] The bulk instability has been observed only for $A>56$ and engenders patterns in the form of spiral waves.[8] For $A=O(1)$ and $s=0$, attention was focused on the possible formation of axisymmetric recirculation bubbles on the cylinder axis called vortex breakdown. These bubbles are not associated with an instability but rather with a smooth change of the basic state. Their axisymmetry breaking is now questioned both experimentally and numerically.[13–19]

The flow between counter-rotating disks $s<0$ has recently revealed a new instability mechanism arising in the free shear layer lying between two regions of opposite azimuthal velocities. Lopez *et al.*[20] have varied $s$ between 0 and −0.8, for $A=2$ and $\mathrm{Re}\equiv\Omega_{\mathrm{up}}H^2/\nu=250$ (with $\nu$ the kinematic viscosity) and have observed rotating waves in the form of funnel-like vortices with azimuthal wave numbers 4 and 5, as well as more complicated dynamics.[21] For $A=20.9$, Gauthier *et al.*[22] also observed a new pattern of spirals, characterized by a wave number between 9 and 11. A possible connection between the funnel-like vortices and the spirals was suggested[22] and eventually confirmed[23] by an experi-

[a)]Electronic mail: nore@limsi.fr

 

mental investigation in the range $A \in [3.8, 20.9]$ and $s \in [-1, -0.135]$, in which the pattern consists of vertical vortices surrounded by a set of spiral arms. At moderate $A$ and large Reynolds numbers, the vortices dominate, while at large $A$, the spirals are preferred.

In previous papers,[24,25] we have studied the exactly counter-rotating case, $s=-1$ with a stationary wall, for different aspect ratios. For $A=0.5$, when the disk rotation rate is increased, the axisymmetric basic state becomes unstable through a transition which resembles the Kelvin-Helmholtz instability of the equatorial azimuthal free shear layer created by the counter rotation of the upper and lower disks.[24] This instability gives rise to steady states with one or two corotating radial vortices and is accompanied by more complex dynamics such as traveling waves, modulated traveling waves, and near-heteroclinic cycles. We have also investigated the linear thresholds[25] over the aspect ratio range $A \in [1/3, 2]$ with azimuthal wave number $m \leqslant 5$. For this aspect ratio range, the nonaxisymmetric modes are dominant and stationary, and the critical azimuthal wave number is an increasing function of $A$. We have identified different codimension-2 points when two adjacent wave numbers $m$ and $m+1$ bifurcate simultaneously. The axisymmetric modes become unstable via stationary or Hopf bifurcations at higher thresholds.

The main purpose of this paper is to complete the numerical linear study for large aspect ratios keeping $s=-1$, i.e., the lower and upper disks are exactly counter-rotating, and to perform a nonlinear investigation at $A=15$ both numerically and experimentally. The outline of the paper is as follows: in Sec. II, the problem is formulated, along with its symmetries. Section III summarizes the numerical methods and code validation. Section IV describes the experimental setup and visualization and measurement systems. In Sec. V the axisymmetric and nonaxisymmetric thresholds for bifurcations from the basic axisymmetric state are reported, together with the patterns of the eigenvectors. It is shown that three-dimensional (3D) modes are not dominant at large aspect ratios. Comparisons between numerical and experimental results are performed in Sec. VI for $A=15$. Section VII contains our conclusion.

## II. FORMULATION OF THE PROBLEM

### A. The governing equations

We consider a cylindrical cavity of height $H$ and radius $R$ filled with an incompressible fluid of kinematic viscosity $\nu$ and density $\rho$. The motion is driven by the upper and lower disks rotating at constant angular velocity $\Omega_{\mathrm{up}}$ and $\Omega_{\mathrm{low}}$, respectively. The dimensionless momentum and continuity equations read

$$\frac{\partial \boldsymbol{V}'}{\partial t} + (\boldsymbol{V}' \cdot \boldsymbol{\nabla})\boldsymbol{V}' = -\nabla p' + \frac{1}{\mathrm{Re}}\boldsymbol{\nabla}^2 \boldsymbol{V}', \tag{1a}$$

$$\nabla \cdot \boldsymbol{V}' = 0, \tag{1b}$$

where $\boldsymbol{V}'$ is the velocity, $p'$ the pressure, and $\mathrm{Re}=\Omega_{\mathrm{up}}H^2/\nu$ the Reynolds number. The velocity, pressure, length, and time are nondimensionalized by $\Omega_{\mathrm{up}}H$, $\rho(\Omega_{\mathrm{up}}H)^2$, $H$, and $1/\Omega_{\mathrm{up}}$, respectively. Two additional nondimensional parameters are the aspect ratio $A=R/H$ and the angular velocity ratio $s=\Omega_{\mathrm{low}}/\Omega_{\mathrm{up}}$. We study the case where the disks rotate at exactly opposite angular velocities, namely $s=-1$, and vary the aspect ratio. The flow geometry is sketched in Fig. 1.

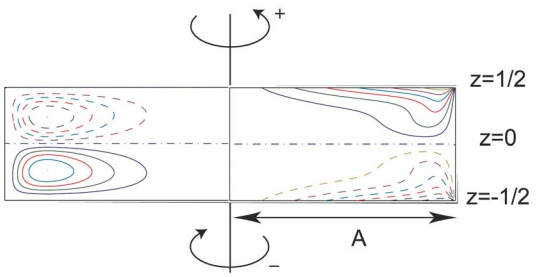


FIG. 1. Sketch of the flow geometry in nondimensionalized units. The inset illustrates azimuthal velocity contours (right) and the streamfunction contours (left) of the axisymmetric flow for $A=2$ and $\mathrm{Re}=120$. For all figures, positive (negative) contours are represented by solid (dashed) lines.

The boundary conditions on the cylinder walls are

$$\boldsymbol{V}' = 0 \quad \text{on the steady sidewall at } r = A, \tag{2a}$$

$$u' = w' = 0 \quad \text{on both disks at } z = \pm 1/2, \tag{2b}$$

$$v' = -r \quad \text{on the lower disk at } z = -1/2, \tag{2c}$$

$$v' = r \quad \text{on the upper disk at } z = 1/2, \tag{2d}$$

where $(u', v', w')$ are the components of the velocity $\boldsymbol{V}'$ in cylindrical coordinates $(r, \theta, z)$.

### B. Symmetries

Figure 1 depicts the basic axisymmetric steady flow. It consists of an equatorial shear layer separating two regions with opposite senses of azimuthal velocities due to the counter-rotating disks (see right-hand side of Fig. 1). Ekman pumping in the neighborhood of each disk creates two recirculation zones shown by streamfunction contours (see left-hand side of Fig. 1).

The geometry and basic state are axisymmetric, i.e., invariant under rotation by any angle $\theta$ about the cylinder $z$ axis, which we denote by $S_\theta$. The present case of exactly counter-rotating disks is unique in possessing an additional symmetry of rotation of $\pi$ about any horizontal axis in the equatorial plane, for example, the $x$ axis. We denote by $R_\pi$ this rotation which is equivalent to combined reflections in $\theta=0$ and in $z=0$. These symmetries are represented by

$$S_{\theta_0}\begin{pmatrix} u' \\ v' \\ w' \end{pmatrix}(r, \theta, z) \equiv \begin{pmatrix} u' \\ v' \\ w' \end{pmatrix}(r, \theta + \theta_0, z), \tag{3a}$$

$$R_\pi \begin{pmatrix} u' \\ v' \\ w' \end{pmatrix}(r,\theta,z) \equiv \begin{pmatrix} u' \\ -v' \\ -w' \end{pmatrix}(r,-\theta,-z). \tag{3b}$$

The main point is that rotation about the $z$ axis and about a horizontal axis do not commute, and hence, the group generated by the operators $S_\theta$ and $R_\pi$ is isomorphic to $O(2)$.

## III. NUMERICAL METHODS

Our goals are to carry out a linear stability analysis of the counter-rotating disk system for a large range of aspect ratios and to compare experimental and numerical nonlinear results for a fixed aspect ratio. We have used different codes based on several computational techniques: a steady-state solver, the ARPACK library[26] to compute leading eigenvalues and a nonlinear nonaxisymmetric code. The main features of these tools are summarized here. Further details can be found in Refs. 24, 25, 27, and 28.

### A. Spatial discretization

The flow fields are represented in cylindrical coordinates $(r,\theta,z)$. Fourier expansions are used in the $\theta$ direction, while a uniform grid is used in the $z$ direction with $N_z+1$ gridpoints and a nonuniform grid with $N_r+1$ gridpoints is used in the $r$ direction.

The grid is refined at the lateral boundaries by placing gridpoints at

$$r_i = A\frac{\tanh\left(\frac{\beta i}{N_r}\right)}{\tanh(\beta)} \quad i=0,\ldots,N_r, \tag{4}$$

where $\beta=1$ for $A<10$ or $\beta=2$ otherwise.

### B. Axisymmetric steady states

Axisymmetric base flows are represented by the azimuthal velocity $V$ and the streamfunction $\Psi$ defining the radial $U$ and vertical $W$ velocities

$$U=\frac{1}{r}\frac{\partial\Psi}{\partial z}, \quad W=-\frac{1}{r}\frac{\partial\Psi}{\partial r}. \tag{5}$$

The axisymmetric basic velocity is then $\boldsymbol{V}(r,z)=[U(r,z),V(r,z),W(r,z)]$. The streamfunction $\Psi$ must satisfy homogeneous Dirichlet (no through-flow) and Neumann (no-slip) boundary conditions, while the azimuthal velocity $V$ obeys the boundary conditions given in (2a)–(2d). The symmetry operator $R_\pi$ acts on this representation via

$$R_\pi \begin{pmatrix} \Psi \\ V \end{pmatrix}(r,z) \equiv \begin{pmatrix} -\Psi \\ -V \end{pmatrix}(r,-z). \tag{6}$$

Thus, modes which are symmetric under $R_\pi$ are represented by scalar functions $\Psi$ and $V$ which are odd functions of $z$. The azimuthal vorticity has the same symmetry properties as $\Psi$. These properties may be used in order to perform computation on half of the domain $0\leqslant r\leqslant A$, $0\leqslant z\leqslant 1/2$. The steady-state solutions are computed using a Newton-Raphson algorithm.[28]

### C. Linear stability analysis and nonlinear integration

A nonaxisymmetric code using primitive variables carries out linear stability analysis of a previously computed axisymmetric steady state $\boldsymbol{V}$ (Ref. 28). For this purpose, the velocity is written in the following form:

$$\boldsymbol{V}'(r,\theta,z,t)=\boldsymbol{V}(r,z)+\epsilon\,\mathrm{Real}[\boldsymbol{v}(r,\theta,z,t)]. \tag{7}$$

Here $\epsilon$ is a small parameter and $\boldsymbol{v}(r,\theta,z,t)$ is a superposition of complex normal modes

$$[u(r,z),v(r,z),w(r,z)]\exp(\lambda t-im\theta), \tag{8}$$

where $(u,v,w)$ are complex functions, $\lambda=\lambda_r-i\lambda_i$ is the eigenvalue with the growth rate $\lambda_r$ and the oscillation frequency $\lambda_i$, and $m$ is the azimuthal mode. The pressure is expanded as one of the velocity components.

The linearized Navier-Stokes equations read at order $\epsilon$:

$$\frac{\partial\boldsymbol{v}}{\partial t}+(\boldsymbol{V}\cdot\boldsymbol{\nabla})\boldsymbol{v}+(\boldsymbol{v}\cdot\boldsymbol{\nabla})\boldsymbol{V}=-\nabla p+\frac{1}{\mathrm{Re}}\boldsymbol{\nabla}^2\boldsymbol{v} \tag{9a}$$

$$\nabla\cdot\boldsymbol{v}=0, \tag{9b}$$

where homogeneous boundary conditions are imposed on $\boldsymbol{v}$. Equations (9) and boundary conditions (2a)–(2d) are discretized by a standard second-order accurate finite difference scheme. The resulting discrete systems for the perturbations lead to a generalized eigenvalue problem. For each azimuthal wave number $m$, the search for the leading eigenvalue (with the largest real part), $\lambda(m,\mathrm{Re},A)=\lambda_r(m,\mathrm{Re},A)-i\lambda_i(m,\mathrm{Re},A)$, is performed with the help of the shift-invert spectral transformation method implemented in the ARPACK library.[26] The procedure to find the neutral Reynolds number $\mathrm{Re}_m(A)$, satisfying $\lambda_r[m,\mathrm{Re}_m(A),A]=0$, is an iterative search for the roots of the real part of the leading eigenvalue. The critical Reynolds number of the flow for each $A$ is $\mathrm{Re}_C(A)\equiv\min_m\mathrm{Re}_m(A)$. The value of $m$ corresponding to $\mathrm{Re}_C(A)$ is the critical mode $m_C$. Validations of the linearized code can be found in Ref. 28.

A nonaxisymmetric code using primitive variables computes the nonlinear time evolution of (1) with a second-order implicit discretization of the linear terms and explicit Adams-Bashforth-type extrapolation of the nonlinear terms.[24] The velocity-pressure coupling is handled by means of an incremental projection method.[30,31] The velocity vector and the pressure are split into their basic and fluctuating parts. The results presented in this paper span the aspect ratio interval $A\in[2,20]$. Validations of the nonlinear code are reported in Refs. 24 and 25.

Runs are performed on a NEC-SX5 computer. The resolution used for computing $m=0$ thresholds is $N_r=301$, $N_z=61$ for half of the domain $0\leqslant r\leqslant A$, $0\leqslant z\leqslant 1/2$ for all aspect ratios. An axisymmetric run to find the basic state and 20 eigenvalues takes about 1.5 min. The resolution used for computing $m\neq 0$ thresholds for each $A$ is specified in Sec. V B. A typical run to find the basic state and 20 eigenvalues with $N_r=257$, $N_z=101$ for the whole domain takes about 5 min. Nonlinear computations are performed with $N_r=385$,

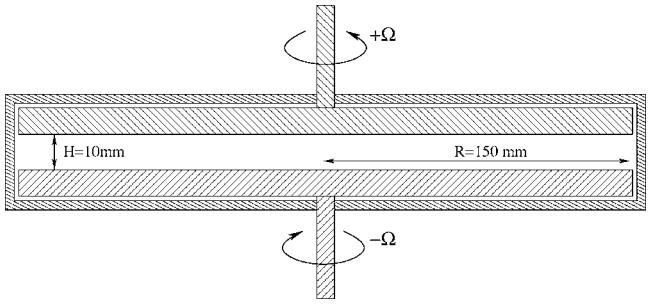


FIG. 2. Experimental device. The aspect ratio is fixed to $A=R/H=15$.

$N_\theta=74$, $N_z=129$, and the time step is $\Delta t=2\pi\ 10^{-3}$ nondimensional time units. A nonlinear run of 100 nondimensional time units takes 8.6 h at 6.3 GFlops.

## IV. EXPERIMENTAL SETUP

### A. Experimental cell

The experimental cell is sketched in Fig. 2. The cylindrical container, made of Altuglas, is mounted vertically. The two glass disks, of radius $R=150$ mm, are driven by two electronically regulated dc motors, and through a system of waterproof ball bearings and gear reducers, they are constrained to rotate in opposite directions. The angular velocity can be set up to $\Omega=2.1$ rad/s with a stability of 0.1%. The distance between the disks, $H$, is adjusted to 10 mm and the aspect ratio is fixed to $A=R/H=15$. The working fluid is water, of kinematic viscosity $\nu=10^{-6}$ m$^2$ s$^{-1}$ at 20 °C. The Reynolds number, $\mathrm{Re}=\Omega H^2/\nu$, is controlled to within 2%.

### B. Velocity measurements and flow visualization

Velocity signals are measured using a laser Doppler velocimetry (LDV) system. This system consists mainly of a 35-mW He-Ne laser (Spectra-Physic), an optical system with a Bragg cell and a front lens (300 mm focal length), and a counter processor (Dantec). A frequency shift is superposed by the Bragg cell onto one of the two laser beams to allow the measurement of very weak and reversing flows. Due to optical deformations of the curved surface, the accessible domain is limited. It is the azimuthal velocity component, which is easier to obtain, that has been measured. The velocity probe has been placed in an area where the instabilities are easier to detect in spite of the difficult optical access: $r/R=0.8$ and $z=-0.08$.

Flow visualizations are obtained by laser tomography in meridional (fixed $\theta$) and horizontal (fixed $z$) planes. Small $TiO_2$ particles are used as a tracer, illuminated by a laser sheet, and photographed. The main difficulty for the meridional visualizations in this geometry arises from the large azimuthal velocity component of the flow perpendicular to the plane, which strongly constrains the time spent by a particle in the laser sheet. In order to get the radial and axial components of the trajectories before particles exit, the sheet was enlarged up to 3 mm. The horizontal plane views near $z=0$ are easier to obtain since the vertical velocity is weak, and then, the particles remain long enough to trace their radial and azimuthal component trajectories. The thickness of the laser sheet was then close to 1 mm.

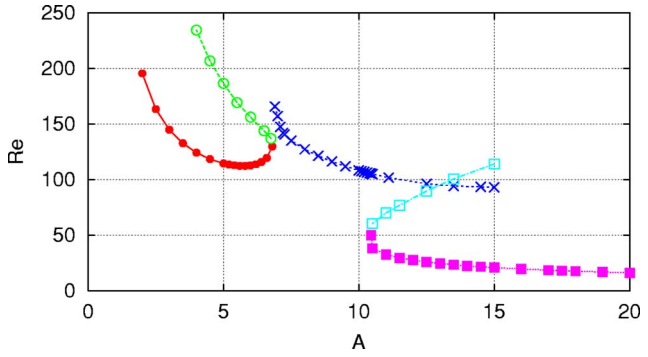


FIG. 3. Axisymmetric thresholds Re as a function of $A$: three stationary bifurcations $P_1$ (●), $P_2$ (○), and $P_3$ (×), and two Hopf bifurcations $H_1$ (■) and $H_2$ (□).

## V. AXISYMMETRIC AND THREE-DIMENSIONAL THRESHOLDS

We study the stability of the flow produced by the counter-rotating disk system as a function of the aspect ratio in the range $2\leqslant A\leqslant 20$ for integer values of the azimuthal wave number up to 15. We compute the critical Reynolds number $\mathrm{Re}_C(A)$ as the lowest Reynolds number, minimized over all $m$, and the corresponding azimuthal mode $m_C$ is the most unstable mode. In the aspect ratio interval under consideration, the azimuthal wave number of the most unstable nonaxisymmetric perturbation increases with $A$ for $A\leqslant 15.5$ and drops to $m=1$ for $A>15.5$. The corresponding instability can be stationary or time dependent and its threshold is the lowest for $A\leqslant 13.25$. The axisymmetric thresholds follow different curves as $A$ is increased: the bifurcation is of pitchfork type for $A\leqslant 10.45$ and of Hopf nature above. The axisymmetric mode becomes critical for $A>13.25$.

### A. Axisymmetric thresholds

We have computed the minimum number of axisymmetric branches for $2\leqslant A\leqslant 20$ and $\mathrm{Re}\leqslant 250$ allowing to understand the evolution of the threshold with $A$. Hence Fig. 3 shows up to three axisymmetric thresholds for each value of $A$. Two pitchfork bifurcations, denoted by $P_1$ and $P_2$, exist for $2\leqslant A\leqslant 6.8$, merging and disappearing in an isola formation point at $A=6.8$, $\mathrm{Re}=129.75$. Another pitchfork bifurcation, denoted by $P_3$, defines the threshold for $6.8<A\leqslant 10.45$. Finally, two Hopf bifurcations, $H_1$ and $H_2$, exist for $10.45<A$ and meet at $A\sim 10.45$, $\mathrm{Re}\sim 50$.

Note that the threshold of the steady branches $P_1$, $P_2$, and $P_3$ is at least twice the threshold of the oscillating $H_1$ branch. Besides, in Sec. VI, we will see that the axisymmetric mode $m=0$ is critical over the 3D modes for $A>13.25$. Therefore, we focus on the leading eigenvector responsible for the $H_1$ bifurcation.

Figure 4 plots contours of streamfunction and azimuthal velocity of the basic state and the eigenvector at $A=15$. The basic state $[\Psi(r,z),V(r,z)]$ is symmetric under $R_\pi$, i.e., the

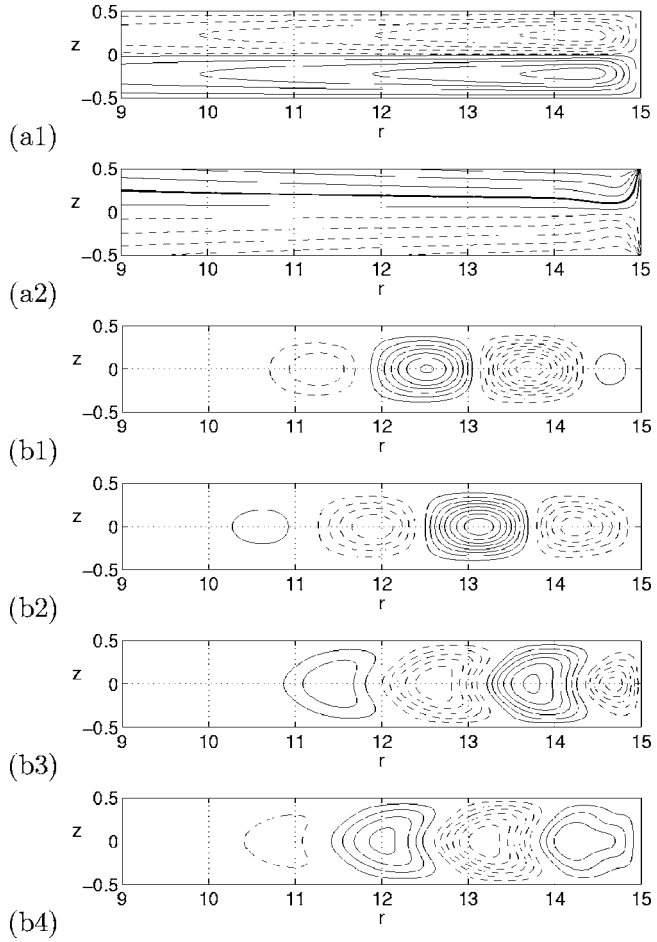


FIG. 4. Streamfunction and azimuthal velocity contours of axisymmetric states for $A=15$ and $9\leqslant r\leqslant 15$. At the bifurcation $H_1$ at $\mathrm{Re}=20.76$: (a1) and (a2) basic state; (b1) and (b2) real and imaginary parts of the streamfunction of the leading eigenpair responsible for the Hopf bifurcation $H_1$; (b3) and (b4) real and imaginary parts of the azimuthal velocity of the leading eigenpair responsible for the Hopf bifurcation $H_1$. The oscillation frequency is $\lambda_i(H_1)=2.39$.

streamfunction and the azimuthal velocity are odd functions of $z$, while the eigenvector breaks this symmetry and is an even function of $z$. We have used this property in order to compute the field in half of the domain, $0\leqslant r\leqslant A$, $0\leqslant z\leqslant 1/2$. (We have observed that eigenvectors with the same symmetry as the basic state are never critical.)

As the leading eigenvalue pair is complex (with $\lambda_i\neq 0$), the real and imaginary parts of the eigenvector are shown and are antisymmetric under $R_\pi$. More precisely, let $\Psi(r,z)$ denote the base state in Fig. 4 (a1), $\psi_0(r,z)$ the real part of the streamfunction of the leading eigenvector in Fig. 4 (b1), $\psi_{T/4}(r,z)$ the corresponding imaginary part in Fig. 4 (b2). Then the small-amplitude limit cycles generated by the Hopf bifurcation $H_1$ can be reconstructed as

$$\begin{aligned}\psi(r,z,t) &= \Psi(r,z)+\epsilon\exp(\lambda_r t)\mathrm{Real}[(\psi_0(r,z)\\ &\quad + i\psi_{T/4}(r,z))\exp(-i\lambda_i t)]\\ &= \Psi(r,z)+\epsilon\exp(\lambda_r t)[\psi_0(r,z)\cos(2\pi t/T)\\ &\quad + \psi_{T/4}(r,z)\sin(2\pi t/T)],\end{aligned}$$

where $T=2\pi/\lambda_i$ is the period and $\lambda_r=0$ at threshold. This form obeys[32] $\psi(r,z,t+T/2)=R_\pi\psi(r,z,t)$. Note that the real $\psi_0$ and the imaginary $\psi_{T/4}$ functions correspond, respectively, to the streamfunction at $t=0$ and $t=T/4$. [The same reasoning applies to (a2) and (b3), (b4) for the azimuthal velocity.] The patterns propagate from the axis towards the periphery and their amplitude increases with the radius. The $H_1$ solution is formed by alternate cells in streamfunction and azimuthal velocity and can be thought as horizontal concentric rolls with alternate azimuthal jets inside.

The physical mechanism for this instability has been presented in Ref. 29 so that we summarize here the main ideas. For large aspect ratio, the critical Reynolds number scales as $A^{-1/2}$. An asymptotic solution for large $A$ gives to the leading order that the Navier-Stokes equations reduce to a formulation in Cartesian coordinates (all curvature terms can be neglected) with an additional centrifugal acceleration, namely $-V^2/r$ in the radial momentum equation. The base flow has then a simple analytical expression except in the end region close to the periphery. The surprising and interesting result is that, even if the amplitude of the perturbation is largest in the end region, the instability can be completely understood when considering the base flow in the core region. The return flow due to $U=0$ at $r=A$ is in fact slightly stabilizing. In the core region, and in the vicinity of a large enough radius, as the curvature terms are neglected, one can think of a direct analogy with the plane Couette flow (which is stable for any Reynolds number for the linear stability analysis). The main difference between both flows is the centrifugal acceleration which has consequences on both the base flow and the perturbation. For the base flow, this acceleration is the driving term in the radial direction, i.e., it is responsible for a nonzero radial velocity. This leads locally to a plane Couette flow velocity profile with a transverse (or spanwise) flow. Nevertheless, this transverse flow is not the crucial ingredient to the instability mechanism. The other consequence of the centrifugal acceleration is that it does couple the azimuthal (or streamwise) velocity perturbation to the radial (or spanwise) velocity perturbation. In the radial component of (9a), the term $(-2vV/r)$ is the source term for the instability and this coupling between radial and azimuthal perturbation velocities is the key to understanding the instability mechanism.[29]

### B. Three-dimensional thresholds

We now turn to the study of nonaxisymmetric modes. Figure 5(a) shows that the critical azimuthal mode $m_C$ first increases with $A$, then "saturates," and finally drops to 1 for $A>15.5$.

For $A\leqslant 5$, the first bifurcation is through a pitchfork bifurcation. The line $m=2A$ has been drawn as a guide as in Ref. 25, where this scaling in $m$ has been proposed as an indication for the Kelvin-Helmholtz instability of the equatorial azimuthal shear layer. Apparently, this behavior extends until $A=3.5$. For $5.5\leqslant A\leqslant 7.5$, the bifurcation is of Hopf type and, for $8\leqslant A\leqslant 15.5$, the bifurcation is again stationary with high critical modes $m_C$ increasing from 8 to 12. For $A>15.5$, the most unstable mode is $m_C=1$ and is time dependent.

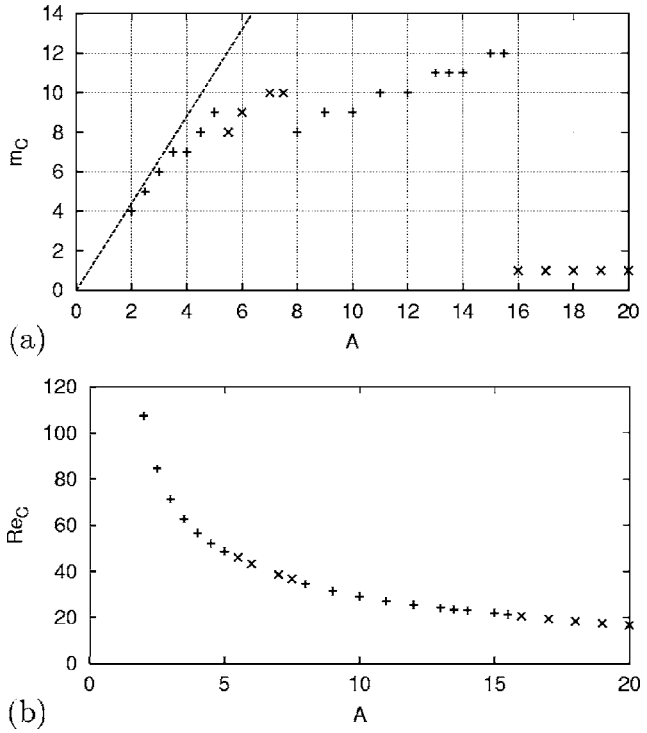


FIG. 5. (a) Critical wave number $m_C$ as a function of $A$ with the indicative dashed line $2A$: + pitchfork bifurcation, × Hopf bifurcation. (b) Critical Reynolds number $\mathrm{Re}_C$ as a function of $A$ realized for different critical wave numbers.

The resolution $N_r \times N_z$ is $257 \times 101$ for $A \leqslant 14$ and $341 \times 101$for $A \geqslant 15.5$. It has been increased for $A=5.5$ and 8 in order to check the change in nature of the bifurcation. The resolution for $A=15$ is the same as the one used to calculate the nonlinear solutions which we will present in Sec. VI.

The critical Reynolds number $\mathrm{Re}_C(A)$ [Fig. 5(b)] corresponding to these critical modes decreases with $A$. Note that this graph is the lower envelope for the curves $\mathrm{Re}_m(A)$ yielding the lowest threshold for each $A$.

We focus on the leading eigenvector at $A=15$ corresponding to a pitchfork bifurcation. We show streamfunction $\Psi$ and azimuthal velocity $V$ of the unperturbed basic state and contours of the velocity field $(u,v,w)$ of the eigenvector at threshold.

As explained in Sec. II B, the symmetry group of the counter-rotating disk system is isomorphic to $O(2)$. When the bifurcation is stationary, each nonaxisymmetric eigenmode is a member of a two-dimensional eigenspace and is associated with a circle pitchfork bifurcation, producing a circle of steady states parametrized by angular phase $\theta_1$ and related to one another by rotation $S_{\theta_0}$. Each eigenmode possesses a horizontal axis of symmetry; its orientation can be chosen so as to make the eigenmode symmetric under $R_\pi$. We have then normalized the eigenvectors so that $v_r[r=(N_r-2)A/N_r, \theta=0, z=0]=1$, where $v_r(r,\theta,z)$ denotes the radial velocity of the eigenvector when the leading eigenvalue is zero at threshold ($\lambda_r=\lambda_i=0$), i.e., for a pitchfork bifurcation. The total radial component reads

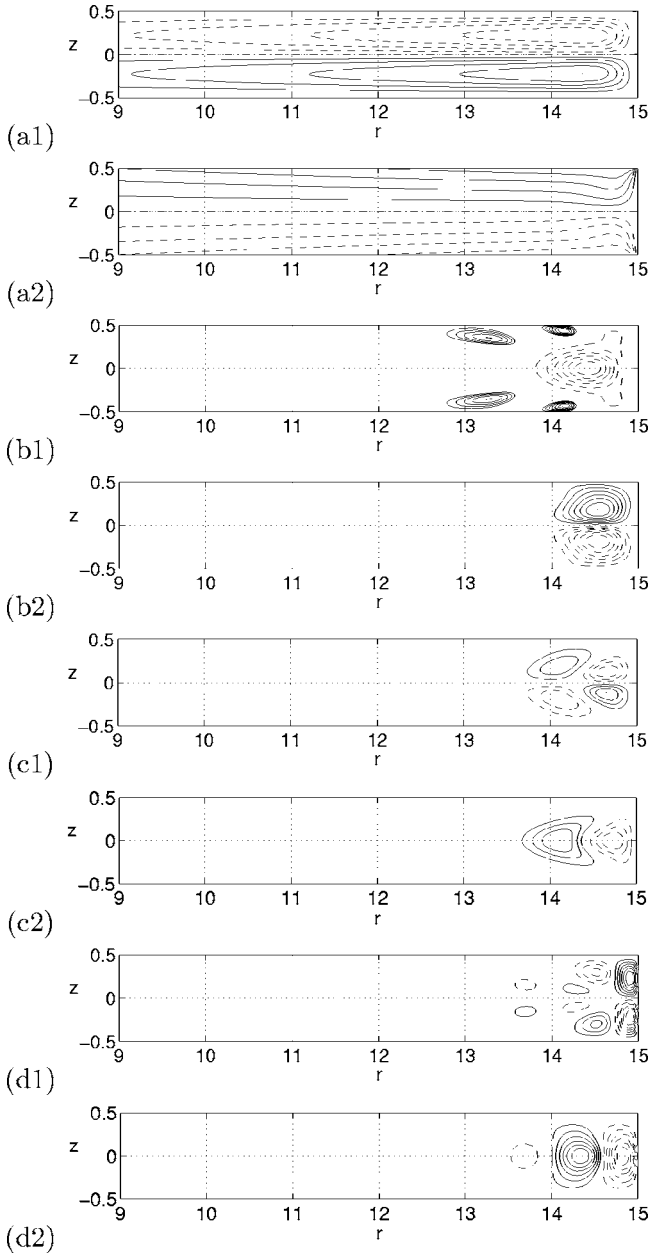


FIG. 6. The $m=12$ eigenvector for $A=15$ and $9 \leqslant r \leqslant 15$ at pitchfork bifurcation at $\mathrm{Re}=21.51$: (a1) and (a2) streamfunction and azimuthal velocity contours of basic state; (b1) and (b2) real and imaginary parts of the radial velocity of the leading eigenvector; (c1) and (c2) real and imaginary parts of the azimuthal velocity; (d1) and (d2) real and imaginary parts of the vertical velocity.

$$U'(r,\theta,z,t) = U(r,z) + \epsilon \exp(\lambda_r t) v_r(r,\theta,z)$$

with

$$v_r(r,\theta,z) = \mathrm{Real}[(u^r(r,z) + iu^i(r,z))\exp(-im\theta)]$$
$$= u^r(r,z)\cos(m\theta) + u^i(r,z)\sin(m\theta),$$

where $u^r$, $u^i$ are the real and imaginary parts of the eigenvector radial velocity. The condition that the eigenmode is symmetric under $R_\pi$ leads to

$$u^r(r,z) = u^r(r,-z),\ u^i(r,z) = -u^i(r,-z).$$

The same reasoning leads to

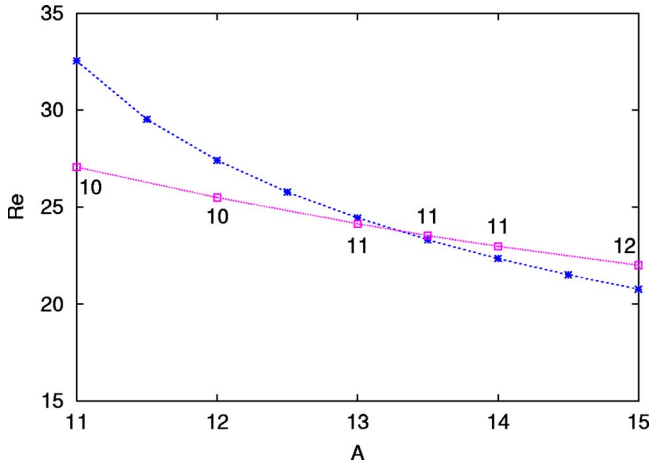


FIG. 7. Crossing of axisymmetric (*) and three-dimensional thresholds (□) at $A=13.25$. The critical 3D mode $m_C$ is indicated.

$$v^r(r,z) = -v^r(r,-z),\ v^i(r,z) = v^i(r,-z),$$

$$w^r(r,z) = -w^r(r,-z),\ w^i(r,z) = w^i(r,-z)$$

for real and imaginary parts of the azimuthal and vertical velocity components. These properties are evident in Fig. 6. Note that the real and imaginary parts of a velocity component correspond, respectively, to the field in the meridional planes $\theta=0$ and $\theta=\pi/2m$. The region of largest magnitude of the eigenvector extends between $3A/4$ and $A$, where the azimuthal shear of the base state is strong.

## VI. ASPECT RATIO $A=15$

We have determined that the axisymmetric mode is critical for $A>13.25$ as shown in Fig. 7.

We perform a study at $A=15>13.25$ both numerically and experimentally in order to analyze the competition between axisymmetric and three-dimensional modes in the nonlinear regime. The $m=0$ mode has the lowest threshold

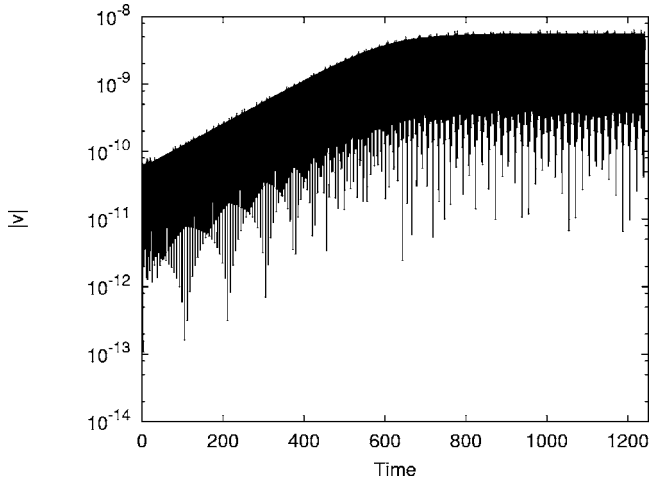


FIG. 8. Time evolution of the fluctuating axisymmetric azimuthal velocity $\log(|v(r=A/10,z=0,t)|)$ from the basic state at $A=15$ and Re=21. Initial phase of exponential growth is followed by a nonlinear phase of slower growth, indicating a supercritical Hopf bifurcation for the $m=0$ mode.

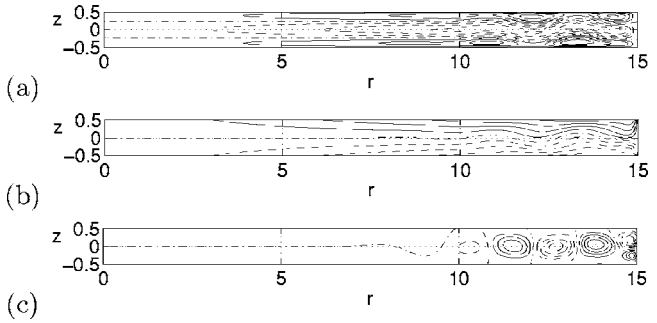


FIG. 9. Contours at Re=23 of the nonlinear axisymmetric oscillating state: (a) the radial velocity $-1.4<u<1.4$, (b) the azimuthal velocity $-15<v<15$, (c) the vertical velocity $-0.7<w<0.8$.

$\mathrm{Re}_c(m=0)=20.76$ and is associated with a Hopf bifurcation. It competes with the $m=12$ mode engendered by a pitchfork bifurcation whose threshold is $\mathrm{Re}_c(m=12)=21.51$.

### A. Nonlinear axisymmetric numerical results

For $A=15$, the axisymmetric bifurcation is a Hopf bifurcation with $\mathrm{Re}_C(m=0)=20.76$ and $\lambda_i=2.39$. The leading eigenvector is represented in Fig. 4 (b1–b4). The motion of the fluctuating part corresponds to meridional rolls propagating centrifugally and crossed by alternate equatorial azimuthal jets. The amplitude of these rolls increases with $r$. We have determined that this bifurcation is supercritical, by temporally integrating the system near threshold (Re=21) from the basic state.[33] Figure 8 shows that the evolution of the absolute value of the fluctuating azimuthal velocity $|v(r=A/10,z=0,t)|$ follows a linear phase until $t\simeq 500$ and that, subsequently, when nonlinear effects come into play, the slope decreases. The $|v|$ velocity shown in Fig. 8 can be thought as representing the amplitude $a$ of the bifurcating mode in a normal-form model $\dot{a}=\mu a+\alpha a^3$. The fact that the slope decreases after the linear phase of the evolution shows that $\alpha$ is negative, thus proving that the axisymmetric Hopf bifurcation is supercritical. We have also performed an axisymmetric nonlinear computation at Re=23. The total velocity field is shown in Fig. 9: it corresponds to the basic state superimposed with the fluctuating concentric rolls propagating centrifugally leading to a wavy motion. Note that the vertical velocity field is dominated by its fluctuating part in the main part of the cavity (where it is nearly even in $z$) since it changes sign only on the border (where it is nearly odd in $z$) in Fig. 9(c).

This axisymmetric mode characterized by $\mathrm{Re}_C(m=0)=20.76$ can compete with the stationary $m=12$ mode for which $\mathrm{Re}_C(m=12)=21.51$ as well as with a collection of

TABLE I. Critical Reynolds number $\mathrm{Re}_C(m)$ for different azimuthal modes $m$ at $A=15$ for pitchfork bifurcations for $m=9,\ldots,15$ and Hopf bifurcation for $m=1$ ($\lambda_i=2.47$).

| $m$ | 1 | 9 | 10 | 11 | 12 | 13 | 14 | 15 |
|---|---|---|---|---|---|---|---|---|
| $\mathrm{Re}_C$ | 22.21 | 22.60 | 21.85 | 21.58 | 21.51 | 21.61 | 21.85 | 22.53 |

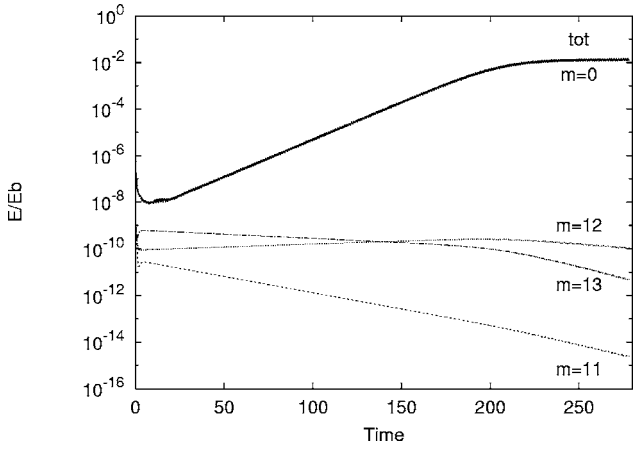


FIG. 10. Time evolution of dominant fluctuating energies $E/Eb$ normalized by the basic state energy at $A=15$ and Re=21.52: "tot" stands for the total fluctuating energy, $m=0,11,12,13$ for the modal energy as indicated. The $m=12$ mode grows initially at short times but, eventually, dies.

other stationary or oscillatory $m\neq 0$ modes listed in Table I. The critical eigenmode for $m=12$ is represented in Fig. 6.

### B. Nonlinear three-dimensional numerical results

We have performed full nonlinear numerical simulations at different Reynolds numbers either starting from the basic state perturbed by a random noise of relative amplitude $10^{-3}$ in energy (for Re=21.52 and Re=23), or starting from asymptotic runs at smaller Reynolds numbers (for Re$\geqslant$24).

For Re=21.52, Fig. 10 shows that the $m=0$ mode is dominant at the asymptotic regime while the $m=12$ mode first slightly increases and then dies. The adjacent modes $m=11$ and $m=13$ decrease as expected. The resulting flow is an axisymmetric centrifugal wavy oscillation shown in Fig. 11. A velocity signal at an arbitrary point is harmonic with a frequency $\lambda_i\simeq 2.38$, comparable to the critical frequency of the $m=0$ mode at Re=20.76 [see Fig. 12(a)].

Time evolution of dominant modal energies is shown in Figs. 13 and 14 for Re=23. The linear growth rate $\lambda_r$ for $m=8,\ldots,17$ of Fig. 15 has a maximum for the $m=13$ mode.

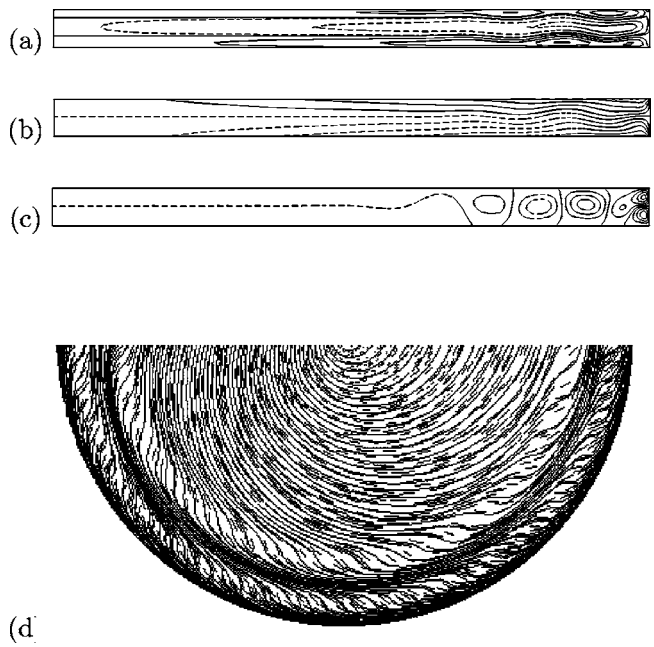


FIG. 11. Nonlinear state at $t=280$ for Re=21.52 and $0\leqslant r\leqslant 15$: contours at $\theta=0$ of (a) the radial velocity $-1.4\leqslant u\leqslant 1.4$ (9 contours), (b) the azimuthal velocity $-15\leqslant v\leqslant 15$ (11 contours), (c) the vertical velocity $-0.9\leqslant w\leqslant 0.5$ (9 contours). (d) Velocity vector in the $z=-0.1$ plane.

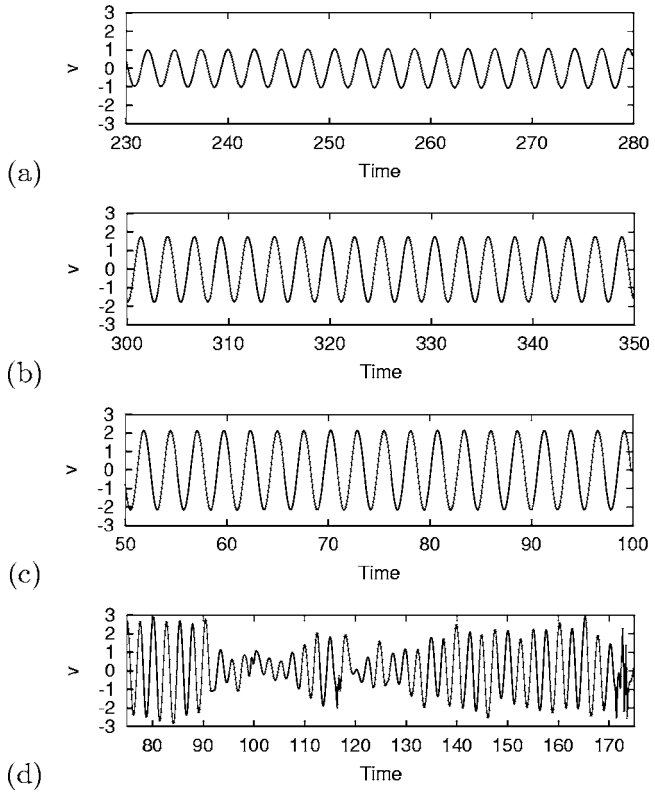


FIG. 12. Time series of the azimuthal velocity $v(r=A/2,\theta=0,z=0)$ for different Reynolds numbers in the asymptotic regime at: (a) Re=21.52 (corresponding to Fig. 10), (b) Re=23 (corresponding to Fig. 14), (c) Re=24, (d) Re=26 (corresponding to Fig. 17). Note that the time series is longer for Re=26 in order to show more signal fluctuations.

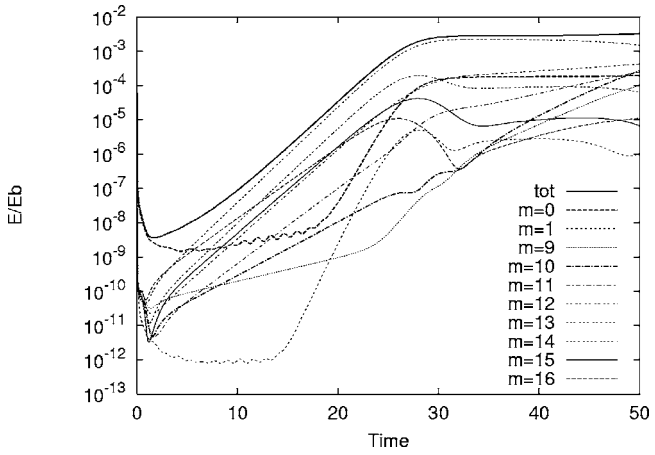


FIG. 13. Short time evolution of dominant fluctuating energies $E/Eb$ normalized by the basic state energy at $A=15$ and Re=23: "tot" stands for the total energy, $m=0$, 1 and $m=9,\ldots,16$ for the modal energy as indicated. The $m=13$ mode (and its harmonics) is dominant at short times.

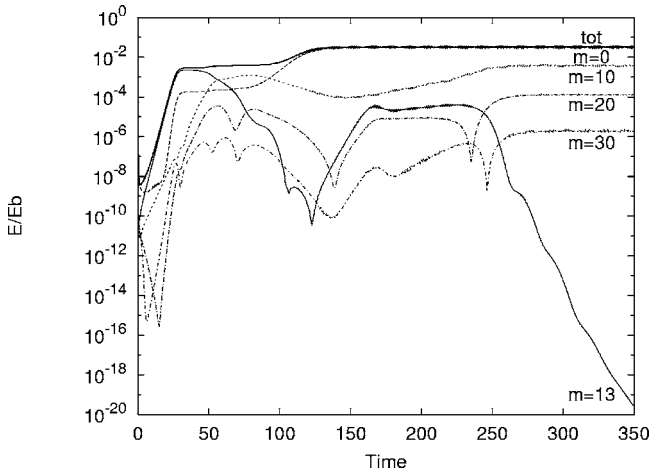


FIG. 14. Long time evolution of fluctuating energies $E/Eb$ normalized by the basic state energy at $A=15$ and Re=23: "tot" stands for the total energy, $m=0,10,13,20,30$ for the modal energy as indicated. The $m=13$ mode (and its harmonics) is dominant at short times, while the $m=0$ and $m=10$ (and its harmonics) modes impose the dynamics at long time.

This growth rate is recovered at short times in the nonlinear computation since Fig. 13 shows the exponential increase of the $m=9,\ldots,16$ modes with the $m=13$ mode being dominant. The $m=0$ mode grows with a slight delay and becomes dominant at $t\simeq 130$. It imposes the oscillations to the velocity signal seen in Fig. 12(b) with again a frequency $\lambda_i \simeq 2.38$. The $m=9,\ldots,16$ modes are populated but, in the steady state, only $m=10$ and its harmonics remain and contain about 10% of the total fluctuating energy. The $m=1$ mode also increases with a slight delay but finally decreases at long time. The spatial structure in a horizontal plane at $z=-0.1$ is shown in Fig. 16(d). The three-dimensional effects are localized near the periphery and show a tenfold structure in relation with the $m=10$ excited mode. Contours of the total velocity (sum of the base and fluctuating parts of the flow) of Figs. 16(a)–16(c) show mainly the same patterns as the axisymmetric solution of Fig. 9 in a fixed $\theta$ plane. This implies that three-dimensional effects are weak and confined to the peripheral region. In fact, in the region $r<0.8A$, the fluctuating flow is nearly axisymmetric and consists of counter-rotating concentric rolls separated by a spatial wavelength $\lambda\sim 2.6$. These rolls propagate radially outwards from the center to the rim which is reminiscent from the waviness motion of the $m=0$ mode.

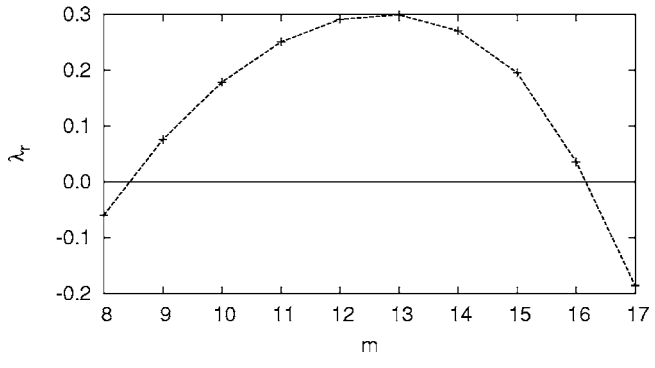


FIG. 15. Linear growth rate $\lambda_r$ for $m=8,\ldots,17$ at Re=23.

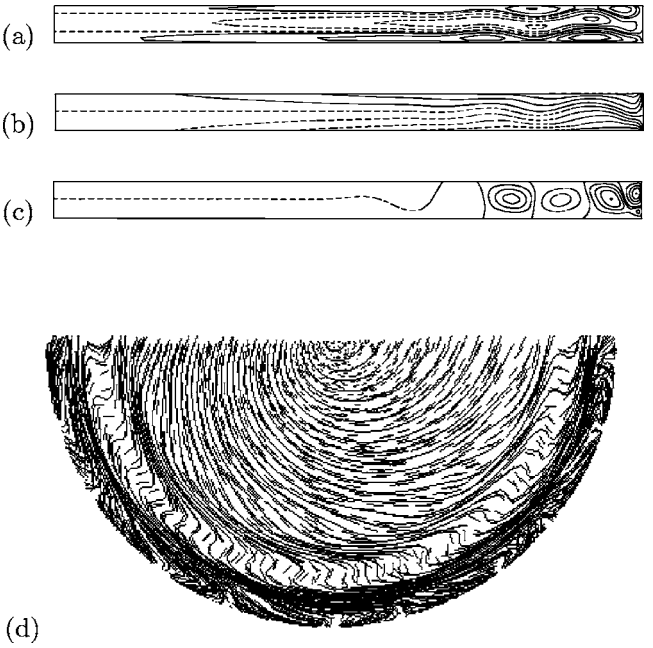


FIG. 16. Nonlinear state at $t=350$ for Re=23 and $0\leqslant r\leqslant 15$: contours at $\theta=0$ of (a) the radial velocity $-1.4\leqslant u\leqslant 1.4$ (9 contours), (b) the azimuthal velocity $-15\leqslant v\leqslant 15$ (11 contours), (c) the vertical velocity $-0.9\leqslant w\leqslant 0.5$ (9 contours). (d) Velocity vector in the $z=-0.1$ plane.

Starting from the asymptotic regime at Re=23, the energy time evolution does not show any qualitative change at Re=24, namely the $m=0$ dominates and the $m=10$ mode contains 12% of the total fluctuating energy. A velocity signal shows harmonic oscillations in Fig. 12(c). The oscillation amplitude in Fig. 12 increases with Re for Re=21.52, 23, and 24.

Increasing the Reynolds number to Re=26 changes dramatically the flow: all 3D modes are populated and the velocity signal is no longer harmonic as seen in Fig. 12(d). The signal is highly intermittent and its amplitude fluctuates. No mode dominates the total energy, therefore we present in Fig. 17 the first four modes. Irregular patterns are localized at $r>0.7A$ [see Fig. 18(d)]. Views of Fig. 19 displaying snapshots of the meridional velocity in a fixed $\theta$ plane show that 3D effects act on the boundary patterns. The distance between the cells varies with time.

### C. Experimental results

Experiments have been performed at $A=15$ for different Reynolds numbers. Time series in Fig. 20 show the azimuthal velocity signal measured at $(r=0.8A,\theta=0,z=-0.08)$ for different Reynolds numbers. At Re=22, the signal remains flat in mean, including noise due to the difficulty of measuring very low velocities (of the order of 1 mm/s). At Re=23, a clear oscillation of period $T=2.5\pm 0.1$ appears which is comparable to the numerical one $T=2\pi/\lambda_i\simeq 2.6$ found at Re=21.52, 23, and 24. Therefore the experimental threshold for the Hopf bifurcation is between 22 and 23, in

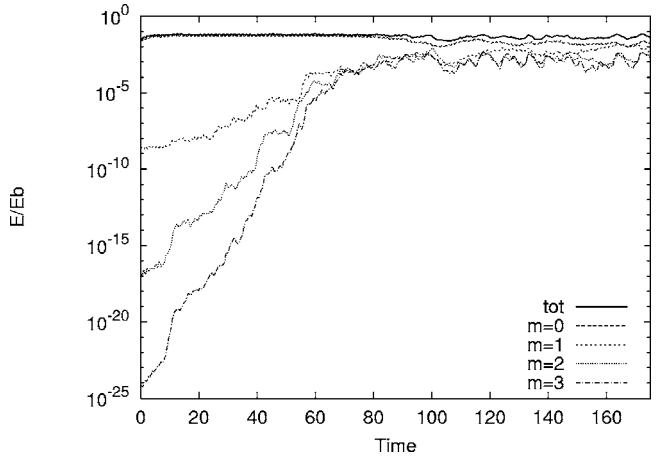


FIG. 17. Long time evolution of fluctuating energies $E/Eb$ normalized by the basic state energy at $A=15$ and Re=26: 'tot' stands for the total energy, $m=0,1,2,3$ for the modal energy as indicated. All three-dimensional modes are populated.

agreement with the numerical threshold $\mathrm{Re}_C(m=0)=20.76$. A similar signal is obtained for Re=24 and 25 with an increasing oscillation amplitude (data not shown). Above Re=25, the signal ceases to be monoperiodic. At Re=28 [Fig. 20(c)], the signal is intermittent showing random fluctuations. These fluctuations, which persist at Re=30 [Fig. 20(d)], are thought to originate from the 3D instabilities invading the domain from the periphery and reaching the measure probe.

Instantaneous meridional visualizations at Re=26 are shown in Fig. 21: upper and lower boundaries correspond to the rotating disks and the fixed lateral wall is on the right. Cells are apparent from $r\simeq A/2$ to the border and propagate

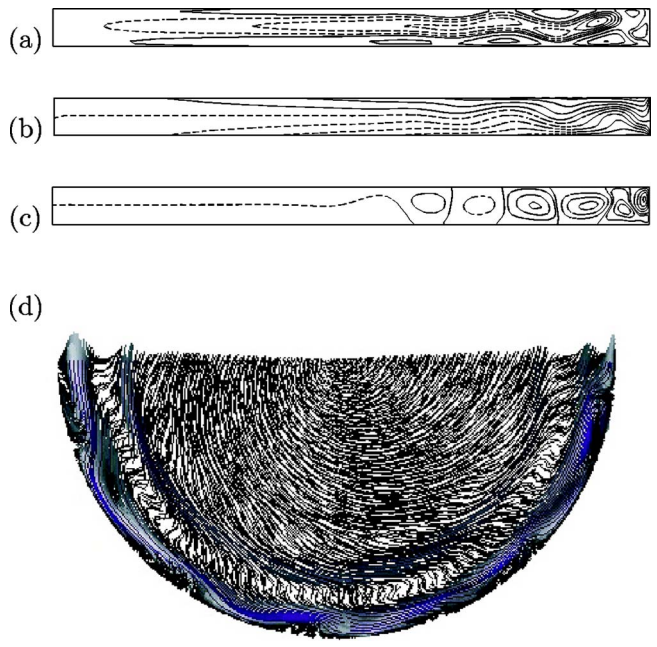


FIG. 18. Same as Fig. 16 at $t=130$ for Re=26 and $0\leqslant r\leqslant 15$.

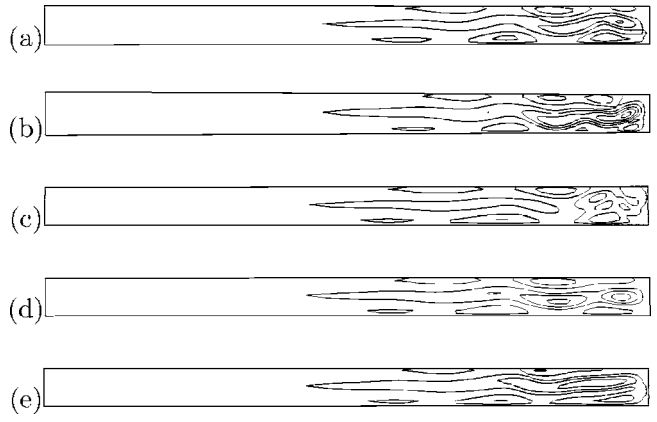


FIG. 19. Contours at $\theta=0$ for Re=26 and $0\leqslant r\leqslant 15$ of the meridional velocity $0\leqslant\sqrt{u^2+w^2}\leqslant 5$ (9 contours) at random instants.

radially outwards in time. The spatial wavelength between rolls greatly varies in time between 1.4 and 2.3 at this Reynolds number as in Fig. 19 in the numerics.

Horizontal visualizations at Re=26 show nearly axisymmetric trajectories near the center [top of Figs. 22(a) and 22(b)] and complicated and intermittent patterns near the wall [bottom of Figs. 22(a) and 22(b)].

The fact that both the time series (Figs. 12 and 20) and flow visualizations [Figs. 19 and 21 and Figs. 18(d) and 22] show similar patterns in numerical and experimental results confirm that there exists a competition between axisymmetric and 3D modes localized at the periphery $r>0.7A$, at least within the range of Reynolds numbers examined here. The 3D effects are therefore not due to experimental imperfections as previously suspected.[34] Although the linear study has proved that the axisymmetric mode is critical, the nearby 3D modes come into play as soon as the Reynolds number exceeds 7% of the threshold. Nonlinear interactions lead to

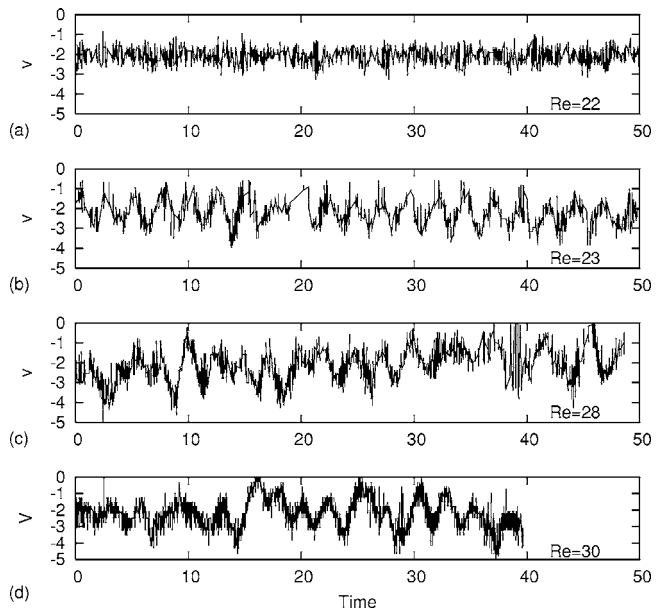


FIG. 20. Time series of the azimuthal velocity $v(r=0.8A,\ \theta=0,\ z=-0.08)$ measured for $A=15$ at: (a) Re=22, (b) Re=23, (c) Re=28, (d) Re=30.

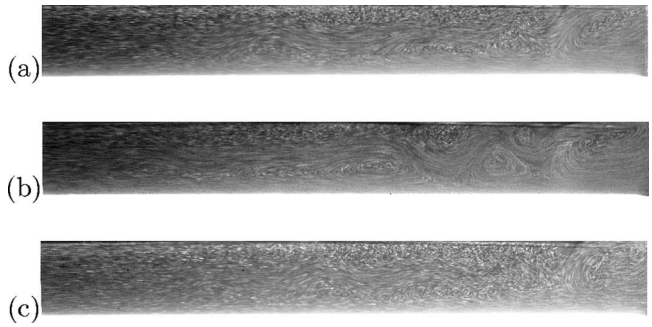


FIG. 21. Instantaneous meridional visualizations at Re=26 for $A=15$ and $0.46A \leqslant r \leqslant A$ or $6.9 \leqslant r \leqslant 15$. The distance between cells varies with time.

complicated and fluctuating patterns, basically axisymmetric near the center and three dimensional at the periphery.

## VII. CONCLUSION

We have numerically and experimentally investigated the dynamics of the exactly counter-rotating von Kármán swirling flow at low Reynolds numbers and at large radius-to-height aspect ratios. Linear computations have revealed that three-dimensional azimuthal modes are dominant at moderate $A$ and that axisymmetric instability prevails at large $A$. Three–dimensional eigenmodes are in general localized near the periphery of the domain and can be stationary or time dependent. Various axisymmetric branches have been investigated and the critical one at large $A$ corresponds to centrifugal wave solutions. The convective or absolute nature of the axisymmetric instability is investigated elsewhere for[29] $s=-1$ and for[34] $-1 \leqslant s < 1$. Nonlinear numerical computations and experimental results at an aspect ratio for which the axisymmetric mode is critical have shown that the proximity of the three-dimensional thresholds leads through complex time evolutions to nonlinear states mixing axisymmetric and 3D modes.

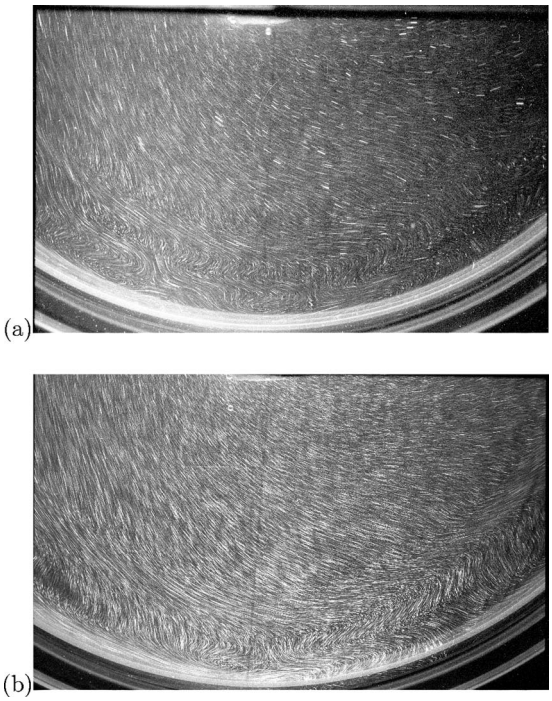


FIG. 22. Experimental plane view near $z=0$ at Re=26 at different times. The experimental device prevents the observation of the whole plan: the maximal radial extension is $0.32A \leqslant r \leqslant A$ or $4.8 \leqslant r \leqslant 15$.

## ACKNOWLEDGMENTS

This work has benefited from fruitful discussions with Laurette Tuckerman, John S. Walker, and Shihe Xin. The computations were carried out on the NEC-SX5 computer of the Institut du Développement et des Ressources en Informatique Scientifique (IDRIS) of the Centre National pour la Recherche Scientifique (CNRS) (Project No. 0254).

[1] P. J. Zandbergen and D. Dijkstra, "Von Kármán swirling flows," Annu. Rev. Fluid Mech. **19**, 465 (1987).
[2] T. von Kármán, "Über laminare und turbulente Reibung," Z. Angew. Math. Mech. **1**, 233 (1921).
[3] G. K. Batchelor, "Note on a class of solutions of the Navier-Stokes equations representing steady rotationally-symmetric flow," Q. J. Mech. Appl. Math. **4**, 29 (1951).
[4] K. Stewartson, "On the flow between two rotating coaxial disks," Proc. Cambridge Philos. Soc. **49**, 333 (1953).
[5] F. Kreith, E. Doughman, and H. Kozlowski, "Mass and heat transfer from an enclosed rotating disk with and without source flow," ASME J. Heat Transfer **85**, 153 (1963).
[6] L. Schouveiler, P. Le Gal, and M.-P. Chauve, "Stability of a traveling roll system in a rotating disk flow," Phys. Fluids **10**, 2695 (1998).
[7] G. Gauthier, P. Gondret, and M. Rabaud, "Axisymmetric propagating vortices in the flow between a stationary and a rotating disk enclosed by a cylinder," J. Fluid Mech. **386**, 105 (1999).
[8] L. Schouveiler, P. Le Gal, and M.-P. Chauve, "Instabilities of the flow between a rotating and a stationary disk," J. Fluid Mech. **443**, 329 (2001).
[9] E. Serre, E. Crespo del Arco, and P. Bontoux, "Annular and spiral patterns in flows between rotating and stationary disks," J. Fluid Mech. **434**, 65 (2001).
[10] A. J. Faller, "Instability and transition of disturbed flow over a rotating disk," J. Fluid Mech. **230**, 245 (1991).
[11] S. V. Pikhtov and E. M. Smirnov, "Boundary layer stability on a rotating disk with corotation of the surrounding fluid," Fluid Dyn. **27**, 657 (1993).
[12] R. J. Lingwood, "Absolute instability of the Ekman layer and related rotating flows," J. Fluid Mech. **331**, 405 (1997).
[13] A. Spohn, M. Mory, and E. J. Hopfinger, "Experiments on vortex breakdown in a confined flow generated by a rotating disk," J. Fluid Mech. **370**, 73 (1998).
[14] F. Sotiropoulos and Y. Ventikos, "Transition from bubble-type vortex breakdown to columnar vortex in a confined swirling flow," Int. J. Heat Fluid Flow **19**, 446 (1998).
[15] F. Sotiropoulos and Y. Ventikos, "The three-dimensional structure of confined swirling flows with vortex breakdown," J. Fluid Mech. **426**, 155 (2001).
[16] H. M. Blackburn and J. M. Lopez, "Symmetry breaking of the flow in a cylinder driven by a rotating end wall," Phys. Fluids **12**, 2698 (2000).
[17] H. M. Blackburn and J. M. Lopez, "Modulated rotating waves in an enclosed swirling flow," J. Fluid Mech. **465**, 33 (2002).
[18] Y. A. Gelfgat, P. Z. Bar-Yoseph, and A. Solan, "Three-dimensional instability of axisymmetric flow in a rotating lid-cylinder enclosure," J. Fluid Mech. **438**, 363 (2001).
[19] J. M. Lopez, F. Marques, and J. Sanchez, "Oscillatory modes in an enclosed swirling flow," J. Fluid Mech. **439**, 109 (2001).
[20] J. M. Lopez, J. E. Hart, F. Marques, S. Kittelman, and J. Shen, "Instability and mode interactions in a differentially-driven rotating cylinder," J. Fluid Mech. **462**, 383 (2002).
[21] F. Marques, A. Y. Gelfgat, and J. M. Lopez, "Tangent double Hopf bifurcation in a differentially rotating cylinder flow," Phys. Rev. E **68**, 016310 (2003).
[22] G. Gauthier, P. Gondret, F. Moisy, and M. Rabaud, "Instabilities of the flow between co and counter-rotating disks," J. Fluid Mech. **473**, 1 (2002).
[23] F. Moisy, O. Doaré, T. Pasutto, O. Daube, and M. Rabaud, "Experimental

and numerical study of the shear layer instability between two counter-rotating disks," J. Fluid Mech. **507**, 175 (2004).
[24]C. Nore, L. S. Tuckerman, O. Daube, and S. Xin, "The 1: 2 mode interaction in exactly counter-rotating von Kármán swirling flow," J. Fluid Mech. **477**, 51 (2003).
[25]C. Nore, M. Tartar, O. Daube, and L. S. Tuckerman, "Survey of instability thresholds of flow between exactly counter-rotating disks," J. Fluid Mech. **511**, 45 (2004).
[26]R. B. Lehoucq, D. C. Sorensen, and C. Yang, *ARPACK User's Guide*, Philadelphia (SIAM, Philadelphia, 1998).
[27]E. Barbosa and O. Daube, "A finite difference method for 3D incompressible flows in cylindrical coordinates," Comput. Fluids **4**, 950 (2005).
[28]L. Martin Witkowski and J. S. Walker, "Solutocapillary instabilities in liquid bridges," Phys. Fluids **14**, 2647 (2002).
[29]L. Martin Witkowski, I. Delbende, J. S. Walker, and P. Le Quéré, "Axisymmetric stability of the flow between two exactly counter-rotating disks with large aspect ratio," J. Fluid Mech. **546**, 193 (2006).
[30]K. Goda, "A multistep technique with implicit difference schemes for calculating two- or three-dimensional cavity flows," J. Comput. Phys. **30**, 76 (1979).
[31]O. Daube, and P. Le Quéré, "Numerical investigation of the first bifurcation for the flow in a rotor-stator cavity of radial aspect ratio," Comput. Fluids **31**, 481 (2002).
[32]Y. A. Kuznetsov, *Elements of Applied Bifurcation Theory* (Springer, New York, 1998).
[33]R. D. Henderson and D. Barkley, "Secondary instability in the wake of a circular cylinder," Phys. Fluids **8**, 1683 (1996).
[34]J. Pécheux and E. Foucault, "Axisymmetric instabilities between coaxial rotating disks," J. Fluid Mech. (to be published).